ARTICLE

Deciphering Helix Assembly in the Heliconical Nematic Phase *via* Tender Resonant X-ray Scattering

Received 00th January 20xx,
Accepted 00th January 20xx

DOI: 10.1039/x0xx00000x

Yu Cao,[a,b] Jun Feng,[b] Asritha Nallapaneni,[b,c] Yuki Arakawa,[d] Keqing Zhao,[e] Huijun Zhang,[a] Georg H. Mehl,[a,f*] Chenhui Zhu,[b*] and Feng Liu[a*]

Being a link between uniaxial nematic and chiral nematic, the twist bend nematic (N_{TB}) has been an intriguing topic over last decade as a key to understand chirality generation. Accurate description and understanding of resonance effects in helical structures provides crucial knowledge on phase behavior beyond positional ordering. We examined the manifestation of resonance effects in N_{TB} *via* tender resonant X-ray scattering (TReXS) at the sulfur K-edge. *For the first time* we demonstrate quantitatively that the energy dependence of the scattering peak in the N_{TB} phase follows the energy dependence of the complex refractive indices measured by X-ray absorption. Taking advantage of molecular energy calculation, we decipher the distinct helical pitch variation trend for symmetric/asymmetric dimers in the perspective of hybridization and reveal the strong effect of substituting oxygen for sulfur atoms on the helical pitch and the thermal helix extension.

1. Introduction

Self-assembled hierarchical structures have emerged as an important class of advanced functional materials due to synergistic and often unique optical, mechanical, electrical and hydrophobic properties and are found both in natural and artificial systems. Helical structures, a subset of hierarchical assemblies, are special. Examples include DNA forming the basis of life, cellulose in trees where helicity imbues mechanical strength, cholesteric liquid crystals (LCs) where the helical pitch defines the observed colours[1-3]. For technological applications of LCs, precise measurement and full control of helicity and associated properties is crucial[4]. Hence the observation of a nematic like LC phase, initially found in chemically non-chiral dimeric molecules and characterized by a pitch ranging typically between 8-12 nm, has garnered significant attention in recent years[5-17], partly due to its potential applications in electro-optical devices[18-21]. A short pitch helix model was proposed, based on electro-optical studies[18, 20], and later confirmed by the Freeze Fracture TEM (FFTEM)[14, 15], Atomic Force Microscope (AFM)[22], Nuclear Magnetic Resonance (NMR)[13], Raman scattering[23], non-resonant hard X-ray scattering[9, 24] as well as C K-edge and Se K-edge resonant X-ray scattering[25-27]. Recently, chirality of the phase was directly measured using synchrotron circular dichroism of aligned samples[28]. Though basic features of this phase are now established, the nature of this phase is still discussed controversially. Existing materials do not behave fully in line with prevailing models[7, 29-31] and alternatives are discussed and supported by experimental data and simulations[32]. Depending on the type of materials, organization in duplexes, pentahedral or octahedral helices has been proposed[27, 33, 34]; the precise measurements of the twisting and tilting of linear molecules in these heliconical structures is still lacking despite limited attempts[35]. The somewhat contested nomenclature for the heliconical phase is not focus of this contribution, for simplicity we use the widely used term "N_{TB}".

In order to clarify the self-assembly behaviour and reach a full understanding of the structure-property relationships, *e.g.* spatial variation of molecular orientation essential for the utilization of the existing properties of this phase and the rational design of advanced materials, precise measurement and description of the nanoscale helical organization are required. Conventional X-ray scattering techniques that rely on spatial electron density fluctuations to provide structural details are not sensitive to complex variation of bond orientation or molecular orientation. Resonant X-ray scattering, also known as anomalous X-ray scattering, overcomes the limitations associated with conventional X-ray scattering by taking advantage of the tuneable, often enhanced, scattering contrast near elemental absorption edges. This technique has been used to provide important structural information, such as counterion distribution in DNA/protein conjugates[36, 37], morphology in multi-component copolymers[38], mean molecular orientations at the interfaces of polymer blends[39, 40] and chirality elucidation in helical structures[41]. Recently, resonant soft X-ray scattering (RSoXS) has been demonstrated to be an unique and effective tool to directly probe periodic layer/molecular orientation variation in the bent-core B4 helical nanofilaments[42], N_{TB} phase[25, 27], blue phases[33], double gyroid phase[43], and other novel phases phases[44-46], based on the

[a] State Key Laboratory for Mechanical Behavior of Materials, Shaanxi International Research Center for Soft Matter, School of Materials Science and Engineering, Xi'an Jiaotong University, Xi'an 710049, P. R. China. Email: feng.liu@xjtu.edu.cn, g.h.mehl@hull.ac.uk
[b] Advanced Light Source, Lawrence Berkeley National Laboratory, Berkeley, CA 94720 USA. Email: chenhuizhu@lbl.gov
[c] Department of Polymer Engineering, University of Akron, Akron, OH 44325 USA
[d] Department of Applied Chemistry and Life Science, Graduate School of Engineering, Toyohashi University of Technology, Toyohashi, 441-8580 Japan
[e] College of Chemistry, Sichuan Normal University, Chengdu 610016, P. R. China
[f] Department of Chemistry, University of Hull, Hull HU6 7RX, U.K.
†Electronic Supplementary Information (ESI) available: [details of any supplementary information available should be included here]. See DOI: 10.1039/x0xx00000x

unique bond orientation sensitivity at the Carbon K-edge. Nevertheless, utilization of soft X-rays for structural examination is often associated with practical challenges: (1) due to the low penetration power of the soft X-rays a high vacuum environment for the samples is required and sample thickness is often limited to the submicron scale[47], and (2) the presence of multiple carbon atoms in a single organic molecule may pose a challenge in deciphering local molecular-level interactions and packing. These complications can be circumvented by utilizing more penetrating tender X-rays (1 keV to 5 keV), which covers K-edges of elements such as Na, Mg, P, S, Cl, Si, K, Ti. Therefore, further development of tender resonant X-ray scattering (TReXS) offers great promise for the exploration of complex structures including biomaterials, battery materials, porous metal organic framework, with natural presence of these above elements. TReXS at the S K-edge was previously applied to discover smectic-C* liquid crystal variants[48, 49], however, its applications to other phases have been very limited[50, 51], one reason for which has been the difficulty in quantitative data interpretation and tensor-based scattering pattern prediction.

Here we address this question directly, through our investigations of a set of materials containing liquid crystal dimers with at least one thioether linkage using TReXS. Scattering peaks behave differently for heliconical structure and layered structures (SmA) with opposite X-ray energy dependence. Furthermore, we demonstrate that the dramatic intensity increase for the N_{TB} phase scattering peak near S K-edge is driven by the strong energy dependence of complex molecular scattering factors, $f(E)=f_0+f'(E)+if''(E)$, measurable using X-ray absorption spectroscopy, with a precision significantly better than that computed from atomic form factor data base[47]. Finally, based on precise TReXS pitch temperature dependence, we show *for the first time* that for molecules of similar lengths the distinct bond hybridizations of sulfur or oxygen ethers impact directly on molecular shape, molecular flexibility, opening angles and the heliconical properties. Our findings provide a novel route to reveal key structural information related to bond orientation in a broad class of natural/artificial hierarchical materials and provide a new idea about N_{TB} phase to community.

2. Methods

Tender resonant X-ray scattering

TReXS measurement was performed at the beamline 5.3.1 at the Advanced Light Source, Lawrence Berkeley National Laboratory. The X-ray beam energy was tuned around the S K-edge, 2472 eV, with a channel cut double-bounce silicon (111) monochromator. A two-dimensional Pilatus detector (300K, Dectris, Inc.) was used to collect the scattering patterns, which were subsequently converted to one-dimensional line profiles using the Nika software package[52]. The scattering patterns were viewed with the Xi-Cam interface[53] at the beamline. The sample-detector distance was tuned between 488 mm and 250 mm to access relevant q range. The beam centers and the sample-to-detector distances were calibrated using both silver behenate and 8CB smectic A.

X-ray absorption spectroscopy

X-ray absorption spectroscopy measurement was performed at the beamline 5.3.1 at the Advanced Light Source, Lawrence Berkeley National Laboratory. The X-ray beam energy was tuned around the S K-edge, 2472 eV, with a channel cut double-bounce silicon (111) monochromator. X-ray absorption spectra were measured with a photodiode in transmission mode. The practical energy resolution is about 1 eV. To reduce air attenuation, the sample chamber was kept in a helium gas environment.

DFT computation

The DFT computation was conducted by Gaussian09D1, visualized by Gaussview6 on the basis function of B3LYP/6-311G(d, p). Optimization and scan functions were used to compute the molecular geometry and energy variation. The natural bond orbitals analysis was conducted by NBO3.1 supplied by Gaussian.

3. Results and discussion

Theoretical computation of TReXS pattern

Two classes of liquid crystals were investigated and their phase sequences are listed in Fig. 1. The first one are the cyanobiphenyl (CB) based dimers with sulfur atoms present at the linking positions between the mesogenic groups and the central alkyl chains of molecules CBSC*n*SCB (*n* = 7) and CBSC*n*OCB (*n* = 5 and 7), exhibiting the N_{TB} phase[54, 55]. The second material (FBTBT) is newly synthesized according to a reported method[56] (Scheme S1) exhibiting a SmA phase and has sulfur atoms located in the aromatic cores. The well characterized molecule 8CB (4'-Octyl-4-biphenylcarbonitrile) is rod-shaped as FBTBT but contains no sulfur atoms and was used as a SmA reference.

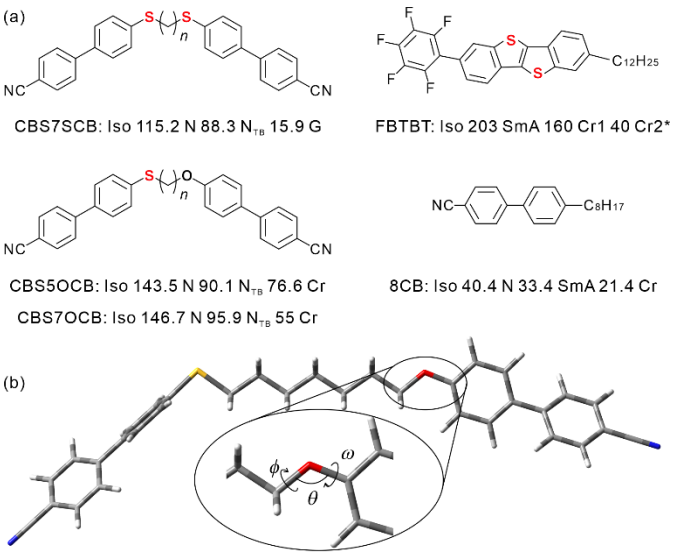

Figure 1 (a) The dimers CBSC*n*SCB and CBSC*n*OCB were reported to exhibit the N_{TB} phase[54, 55]. The newly synthesized sulfur-containing FBTBT exhibited SmA phase, and sulfur-free 8CB was used as a reference for the SmA phase, *n* is the number of repeating -CH_2- units; (b) Stick model of CBS7OCB, the rotation angle, bond angle and dihedral angle are indicated by ϕ, θ and ω, respectively.

The N_{TB} phase of CBSC7SCB exhibited one single scattering peak at q = 0.72 nm^{-1}, which is only visible near the S K-edge (Fig. 2a) and

corresponds to the helical pitch of the N_{TB} phase. The helical pitch increased (decreased in the value of q) as the temperature increased towards the N_{TB}-N transition (Fig. 2b). A similar temperature dependence of the helical pitch was observed in other N_{TB} compounds (Fig. 4). Remarkably, the peak intensity was observed to increase dramatically when the X-ray energy is increased towards the S K-edge (Fig. 2a and Fig. S1). The peak intensity reduced abruptly right after the S K-edge, which was attributed to the increase in absorption of resonant atoms (Fig. S5). All N_{TB} materials examined in this study exhibited strong energy dependence of the scattering peak intensity (Figs. S1 and S8). This observation is qualitatively similar to the one noticed in the N_{TB} phase in CBC7CB[25], B4 helical nanofilaments in NOBOW[42] and three-dimensional cubic phases[33, 43]. However, the energy-dependence of such a 'forbidden' scattering peak originating from periodic bond orientation variation has not been accounted for quantitatively in any previous liquid crystal work and will be discussed below in comparison with the SmA case. There the scattering is expected to be dominated by smectic layering. We note a small discrepancy (~2%) between our measurements and related work[55]. And we attribute this to batch variation, due to synthesis by different research groups.

The SmA phase of the sulfur-containing FBTBT exhibits one peak at q = 2.14 nm^{-1} (Fig. 2c), corresponding to a d-spacing (= $2\pi/q$) of 2.93 nm. This value is very close to the extended molecular length (~3.10 nm), confirming that this peak has its origin from electron density modulation perpendicular to the plane of the layers. Interestingly, the peak intensity decreased noticeably at the S K-edge, which is clearly related to resonant sulfur atoms compared with reference 8CB (Fig. 2c, d) and fundamentally different from the dramatic increase in N_{TB} peak at the S K-edge (Fig. 2a, c). For the crystal phase of CBSC7OCB and FBTBT several scattering peaks were detected at room temperature (Fig. S2c). Especially, there are two sharp peaks at q = 2.04 nm^{-1} and q = 4.08 nm^{-1} for the crystal phase of CBSC7OCB in a ratio of 1:2 representing smectic-like packing. Additionally, TReXS data for the crystal phase of CBSC7OCB contains one pure resonant peak at q = 1.02 nm^{-1}, which matches exactly a double layer distance. Here we focus on the more representative energy-dependence behavior in the SmA and N_{TB} phases, especially on the origin of totally reversed scattering intensity-energy dependence in the vicinity of the S K-edge. Understanding this phenomenon quantitatively would be the first step to a more accurate interpretation of resonant scattering and orientational order.

We adopted the scattering intensity expression[36] represented in Eq. 1 to understand the nature of resonant scattering, wherein the complex scattering factor is given by $f(E)=f_0+f'(E)+if''(E)$ and $v(q)$ represents the spatial distribution of resonant species independent of X-ray energy. This expression reveals that the intensity measured near absorption edge consists of three parts: (1) the first term ($F_0^2(q)$) denotes the non-resonant intensity that is measured from atoms far from their absorption edge; (2) the second term ($2f'(E)F_0(q)v(q)$) corresponds to the cross term of the non-resonant and the resonant part (thus partially resonant), and scales linearly with $f'(E)$; note that $f'(E)$ is negative and accounts for the reduction in the effective number of electrons whereas the term $f_0+f'(E)$ contributes to

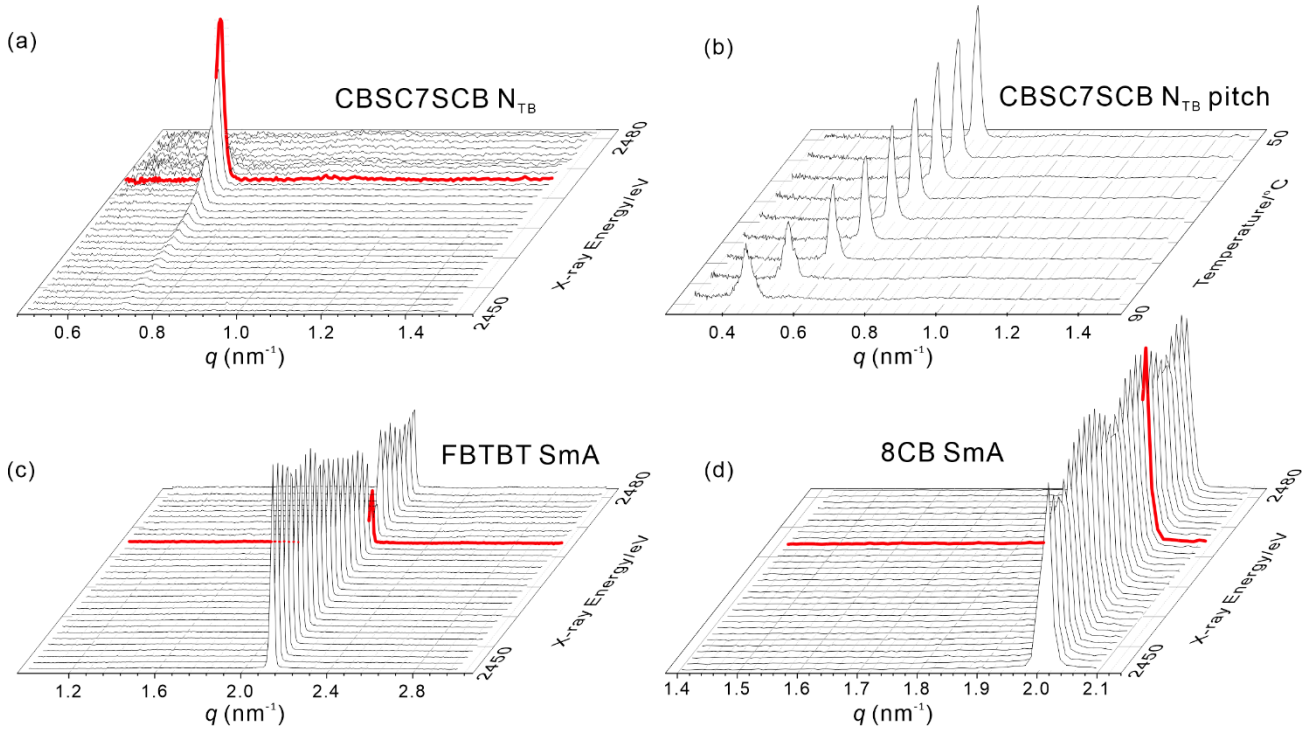

Figure 2 (a) TReXS Energy scan of the N_{TB} phase of CBSC7SCB at 60 ˚C indicates the presence of an energy dependent resonant peak at q = 0.72 nm^{-1}; (b) Temperature scan of the N_{TB} phase at E = 2471 eV upon cooling from 90 ˚C to 50 ˚C. Pitches decreased upon cooling from the nematic phase; (c), (d) TReXS Energy scans of the SmA phase of FBTBT (with sulfur atoms) at 195 ˚C and 8CB (without sulfur atoms) at room temperature, respectively. A sudden intensity dip is observed in the vicinity of S K-edge for FBTBT but not for 8CB, thus, considered partially resonant. Red thick lines correspond to the scattering at E = 2741 eV, slightly below S K edge.

scattering (Fig. S7); (3) the third term, $(f'^2(E)+f''^2(E))v^2(q)$, is based on pure resonant scattering and scales with the sum of $f'^2(E)$ and $f''^2(E)$.

$$\boldsymbol{I_0(q) = F_0^2(q) + 2f'(E)F_0(q)v(q) + (f'^2(E) + f''^2(E))v^2(q)}$$ Eq. 1

First, we checked the case of the SmA phase with the above expression. Based on the experimental data provided in Fig. 2, integrated peak intensities for the SmA and N_{TB} phases as a function of X-ray energy were plotted as shown in Fig. 3. As 8CB contains no sulfur, the observed small fluctuation in integrated intensity is attributed to background fluctuations due to beamline optics (Fig. 3b). The SmA phase in FBTBT shows an additional intensity dip near the S K-edge, which is clearly due to the sulfur atoms present in FBTBT. Given a large non-resonant $F_0^2(q)$ term in the SmA phase of FBTBT (Fig. 3b), the cross term in Eq. 1 contains the leading resonant contribution and therefore should be the main perturbation to the measured scattering intensity. To calculate the contribution of the partial resonant term quantitatively, X-ray absorption spectra near the S K-edge were measured (Fig. S5) to obtain the imaginary dispersion correction, $f''(E)$ from FBTBT (Fig. 3a) following $\mu = 2\rho N_a r_e \lambda f''/m_a$, where μ is the attenuation coefficient, ρ is the density, N_a is the Avogadro constant, r_e is the classical electron radius, m_a is the atomic molar mass, and λ is the X-ray wavelength. Evidently, the experimental imaginary dispersion correction $f''(E)$ near the S K-edge (Figs. 3a, c and Fig. S6) differs significantly from the simulated ones based on the atomic form factor database[47]. In organic molecules, both molecular orbital hybridization and specific local chemical environments affect the details in near-edge absorption spectra. The corresponding dispersive component, $f'(E)$, in the SmA phase of FBTBT, was calculated from $f''(E)$ using the Kramers-Kronig relation[57], and that overlaps with the measured scattering intensity, $I(E)$, reasonably well (Fig. 3b). This is a strong indication that the peak intensity in the SmA case follows the adopted expression as long as the experimental refractive indices (dispersion and absorption), rather than the simulated, are used for the near-edge region.

Next, we discuss the energy dependence of peak intensity for the N_{TB} case, which has so far never been accounted quantitatively for the N_{TB} peak, Smectic-C* variants[48] or other liquid crystal phases where bond orientation variation dominate the phase formation. In the N_{TB} phase, non-resonant SAXS data showed no peak at $q = 2\pi/p$, where p corresponds to the full helical pitch, suggesting that the non-resonant term $F_0^2(q)$ in Eq. 1 is negligible and the electron density modulation from the helical structure is minimal. Fig. 3d also indicates that the observed scattering peak near the S K-edge is due to pure resonance, which agrees with the N_{TB} structural model that

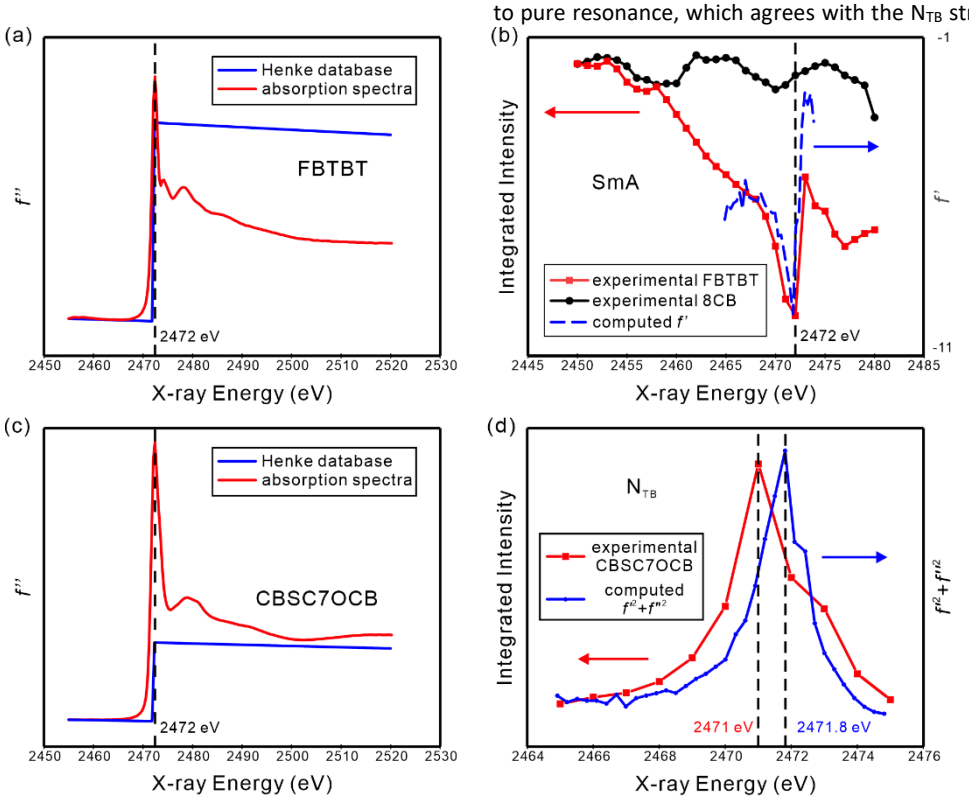

Figure 3 (a) Imaginary part of the dispersion correction (f'') computed from experimental absorption spectra (red) taken in the SmA phase (at 195˚C) and atomic form factor data base (blue) of FBTBT. Significant differences are observed around the sulfur absorption edge (2472 eV); (b) The integrated intensity of the SmA peak of 8CB (black), partially resonant SmA peak for FBTBT (red), and computed real part of the dispersion correction (f') (blue dashed line) *vs* X-ray energy. For comparison, all of intensities of 8CB are scaled by a multiplier constant which was obtained from the intensity of FBTBT and 8CB at E = 2450 eV. A dramatic dip around the S K-edge can be found for FBTBT. The computed f' shows a similar dip at the S K-edge suggesting that the intensity dip in FBTBT arises from resonant sulfur atoms; (c) Computed imaginary part of dispersion correction (f'') from absorption spectra (red) and atomic form factor data base (blue) of CBSC7OCB at 90 ˚C; (d) Experimental integrated intensity of N_{TB} peak of CBSC7OCB (red) and computed scattering contrast ($f''^2+f'''^2$) (blue) *vs* X-ray energy. Experimental data reaches its maximum at 2471 eV with strong energy dependence. Intensity increased dramatically, *i.e.* by a factor of > 23 from 2465 to 2471 eV. Both experimental and computed results exhibit similar trends around absorption edge except for a slight shift attributed to the instrumental resolution limitation.

exhibits periodic bond orientation variation from a screw axis. As reported previously, the precise description of bond orientation sensitivity and structure factor calculation typically requires a treatment of a second rank tensorial form factor[33, 58-60], which can be modelled as a 3 × 3 matrices. This is in the simplest case a traceless diagonal matrix representing tetragonal symmetry with only two unequal parameters, *i.e.* the scattering factors parallel, f_{para}, and perpendicular, f_{perp}, to the molecular long axis or specific chemical bonds of interest. Due to limitations in instrumentation capability and sample preparation challenges, here, we assume a fixed anisotropy in the scattering factor, *i.e.* a constant ratio of f_{perp}/f_{para} independent of X-ray energy. We focus on the general quantitative energy-dependence of such an anisotropy, which is responsible for the pure resonant peaks from periodic orientation variation. Complex dispersion corrections, $f'(E)$ and $f''(E)$ were computed from the measured absorption spectra (Figs. S5-7, Table S1). Fig. 3d indicates that the computed $f'^2(E)+f''^2(E)$ curve matches reasonably well with the results of measured peak intensity as a function of energy (except for a slight shift in the peak position), thus validating the hypothesis that the energy-dependence of the N_{TB} peak intensity basically follows the energy dependence of complex molecular scattering form factors (Fig. S8). We note that a similar expression has been adopted for calculating compositional contrast in multicomponent polymeric systems[61] but has not been extended to systems with pure orientational ordering such as the helical N_{TB} liquid crystals[25, 50], B4 helical nanofilaments[42], blue phases[33], B2 phases[62] or Smectic-C alpha phases[48, 63, 64].

From our theoretical computation, it is clear that the distinct scattering intensity variations in the vicinity of the S K-edge for the SmA and the N_{TB} phases are actually from different scattering sources. For the SmA phase, the scattering signal is from the electron density modulation, scaling with $f'(E)$, which will be absorbed and is weaker in the vicinity of the S K-edge. In contrast, for the N_{TB} phase electron density modulation is absent. Orientation order contributes here to the scattering signal, which will be enhanced around the S K-edge along with the change of $f'^2(E)+f''^2(E)$.

Learning of distinct N_{TB} behaviours

The well-fit quantitative computation and sharp resonant signal just below the $T_{N\text{-}NTB}$ transition (Fig. S9) suggests that TReXS can probe the orientation order with high efficiency close to the phase transition, even when only one or two resonant atoms are embedded in the molecules. With such high-quality data and in-depth understanding of the TReXS, we can decipher the phase behavior in the N_{TB} phase better, especially near $T_{N\text{-}NTB}$. As discussed above, it is surprising that the pitch for both asymmetric dimers (CBSC7OCB, CBSC5OCB) p_{as} was found to be significantly larger than that of the symmetric dimer (CBSC7SCB) p_s, see Fig. 4. Clearly noticeable is the decrease of the helical pitch with lowering the temperature from the nematic/N_{TB} transition temperature. For CBSC7SCB this follows the trend reported for a number of cyanobiphenyl based dimers investigated by RSoXS[25, 33] and is in line too with results for difluorosubstituted dimers using S and Se K-edge resonant scattering[26, 65]. This has been associated with a decreasing number of twisted conformations of the molecules at higher temperatures and a subtle interplay between bent conformations and twisting as a function of the central spacer lengths. At high temperatures, due to temperature induced fluctuations the helical ordering unwinds, the pitch is larger and decreases with lowering the temperature. For most previously investigated systems a pitch ranging typically between 8-12 nm has been reported[25, 26, 33, 50], which is in line with CBSC7SCB. The results for the materials CBSC5OCB and CBSC7OCB follow this general trend, however, they behave qualitatively different to materials reported earlier. The pitch is significantly larger than other dimeric materials, reaching values of 18.4 nm for CBSC7OCB and 14.8 nm for CBSC5OCB respectively, see Fig. S10(a). As the difference in the overall molecular length between CBSC7OCB (3.32 nm) and CBSC7SCB (3.16 nm) is very small, differences in molecular size cannot account for this qualitatively different behavior, having a different molecular origin to that discussed earlier[65]. To understand the molecular origins for this behavior, DFT calculations have been performed based on all-trans models[54, 55]. Calculated differences in the opening angles of the bent shaped molecules of 126° for CBSC7OCB, 109° for CBSC7SCB, respectively, support the view that the different helical behavior is associated with the molecular opening angles, which is also an influential factor on N_{TB} phase range[66]. As shown in Fig. 4, the pitches (p_{as}) of the asymmetric dimers and pitch (p_s) of symmetric CBSC7SCB decreases upon cooling and reached a limit far from the phase transition temperature. Clearly, there is unequal pitch decrement for asymmetric/symmetric dimers upon cooling. By plotting the reduced correlation length, in other words, the number of helical stacks as a function of the reduced temperature shows us that the investigated behavior is rather similar for the investigated systems, 10 °C below the transition the correlation length is equivalent to about 24-28 helical stacks for all materials (see Fig. S10c). This finding suggests that the asymmetric and symmetric dimers are assembled in a similar manner in the heliconical arrays.

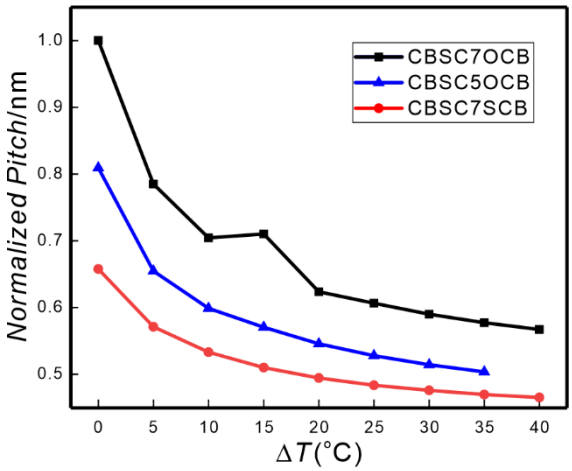

Figure 4 Normalized pitch variation *vs* reduced temperature ($\Delta T = T_{NTB\text{-}N} - T$) in the N_{TB} phase. ΔT denotes temperature difference below the transition temperature from the nematic to N_{TB} phase upon cooling. The pitch decreases more for asymmetric dimers (CBSC7OCB and CBSC5OCB) than symmetric one (CBSC7SCB) upon cooling.

To decipher the phase behaviour upon cooling, a comprehensive DFT calculation on the basis function of B3LYP/6-311G(d, p) was conducted *via* Gaussian G09W and visualized by Gaussview6. Geometry optimization obtained quantitatively similar results as previous studies on sulfur and oxygen contained dimers[55, 67]. Considering the preferential geometry in the ordered liquid crystal[68] and low energy differences, we chose an all-trans model to decipher the structure variation of the N_{TB} phase as shown in Fig. 5.

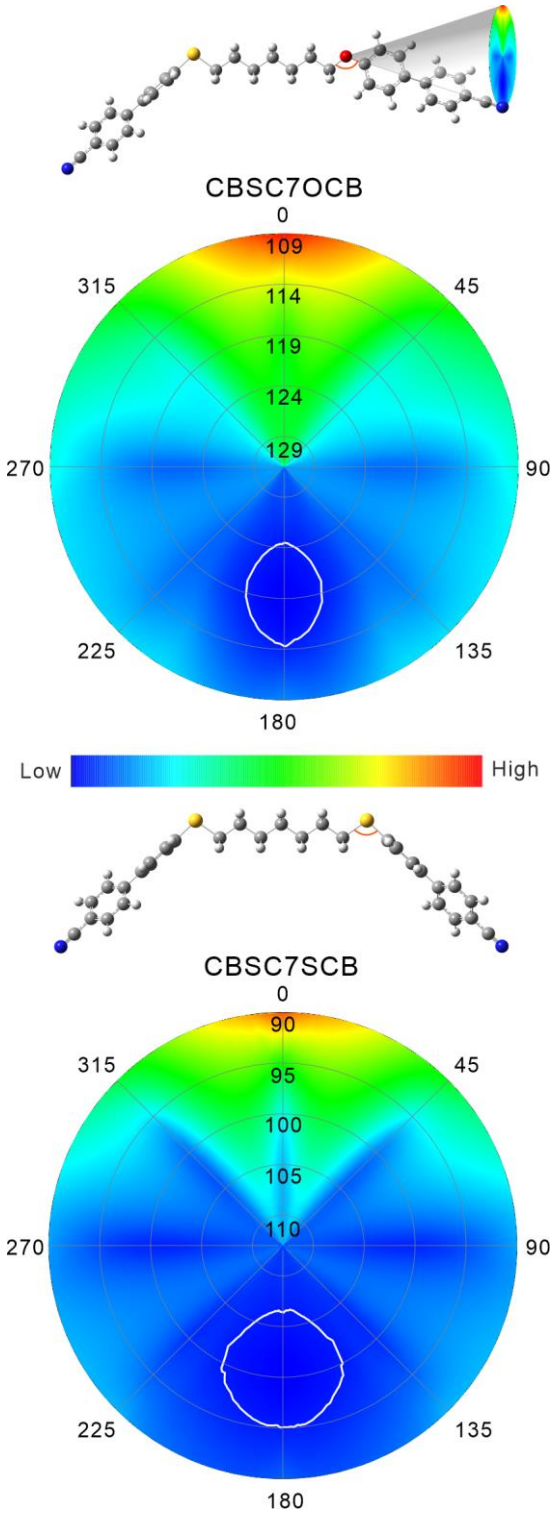

Figure 5 The energetic 2D plots considering bond angle and rotation angle for symmetric/ asymmetric dimers. The concentric circles represent different bond angles and each angular tick stands for one rotation angle. The solid white lines show the acceptance regions for the molecular configurations.

Relaxed and rigid scans are preformed based on the optimized configurations to reveal the critical factors determining the distinct phase behaviors. To understand the subtle difference between two dimers, we focus on the three parameters that could affect the molecular shape, namely, rotation angle ϕ, bond angle θ and dihedral angle ω as shown in Fig. 1b. First of all, relaxed scans, aiming at acquiring lowest energy for fully flexible molecules, of all three parameters are conducted and the optimized energies are plotted in Fig. S11. As anticipated, moving away from the minimum results in monotonic rise of the energy and large changes result in dramatic energy penalties and that is very similar for both systems. For the rotation angle and the dihedral angle, the data shows strong differences between two dimers while the energy landscape is subtler for CBSC7SCB. We immediately notice that the huge difference of the energy barriers of the dihedral angles could induce different behaviors. More precise relaxed scans in steps of 5˚ for the dihedral angle and 2˚ for the bond angle are conducted around the optimized values. To parametrize this, relationships between the angular parameters (ϕ, θ and ω) were plotted in Figs. S12-13 and the Pearson correlation coefficients were determined and are listed in Table S2. We use them to evaluate how influential these parameters are. The correlation between dihedral angle and energy of CBSC7SCB is relatively lower (0.724) when compared with other coefficients (~0.97) indicating that dihedral angle is less influential for the symmetric dimer. Moreover, we estimate the correlation between energy and induced bond/dihedral angle variation. The bond angle induced dihedral angle variation is closely related with energy for both dimers (~±0.9). Yet the correlation between dihedral induced bond angle and energy is much weaker (~±0.6). The analysis suggests that the effect of the bond angle is more pronounced in the dimer system. Taking advantage of the estimated lowest energies upon scans, we could exponentially fit the $\delta\theta$-δE curve, which suggests that the symmetric dimer is more elastic. Furthermore, we derive the elastic constants of two dimers as shown in the supplementary information.

Considering the impact of temperature and Boltzmann constant, the energy provided by temperature would be ~3.1 kJ/mol. We note that such an energy gap supports the symmetric dimer dihedral angle changing freely. But for asymmetric dimer, the dihedral angle is limited to a narrow range centred around 0˚. Upon cooling, the bond angle of CBSC7SCB could increase by ~4˚ whereas for CBSC7OCB it changes by less than 1˚ relating to the induced bond angle variation in Fig. S13(b, d). Bond angle differences would decrease by about 20% to ~16 ˚ upon cooling, we are of the view that this is sufficiently significant to induce the detected increase of helical pitch ratio p_{as}/p_s.

To further value the combined effects of the three parameters, we conducted multi-component rigid scans, which is a method where all configurations are fixed except for the scanned angle, to energetically estimate the acceptance region of dimers'

configuration, see Figs. S14 and S15. Simplified 2D polar maps, whose datasets are chosen as Fig S16, are used to reveal the acceptance region considering bond angle/rotation angle in Fig 5. Overall, the energy of the symmetric dimer is lower than in the asymmetric variant. Though rotation angles do not show a clear correlation with the bond angle as in Fig. S12(b, d), the combined effects of both parameters exhibit a striking influence on molecular shape. Considering the director variation, a larger rotation angle induces a shorter pitch as shown in Fig. S17. From the detailed plotted acceptance region in Fig. S18, we could clearly find that the gradient of symmetric dimer is larger than that of asymmetric dimer, which means that the pitch decrease effect from the rotation angle would vanish faster for CBSC7SCB when compared with CBSC7OCB. This could be another potential reason of increased p_{as}/p_s.

After detailed energetic analysis, we found that both dihedral and rotation angles have a larger acceptance region for the symmetric dimer, which is responsible for the phase behaviour difference. To answer why these angles are easier to rotate in the symmetric dimer, we conducted the Natural Bond Orbital (NBO) analysis. The result indicates that S-C bond is almost non-polar while the O-C bond is rather polar in Tables S3, S4. Moreover, in the perspective of hybridization, the *p* character of sulfur is significantly higher than that of oxygen. The conjugation effect in the O-C bond is due to the sp^2 hybridization of oxygen. This would hinder the free rotation of the sigma bond causing a relatively higher energy difference between the symmetric and asymmetric dimers.

Subsequently we considered the crystal phase of the asymmetric dimer CBSC7OCB. With help of two peaks in the small angle region and the pure resonant peak interpreted as bilayer distance, we reconstructed the electron density map with molecular packing (Fig. S19). Determined from TReXS, the single layer distance is around 3.08 nm, which suggests an intercalated structure as in Fig. S19. The resulted anticlinic molecular packing resembles that formed by 9-(3BEP)2[69]. The results for the crystal phase suggest the asymmetric dimers might form the N_{TB} phase *via* anticlinic packing. Based on the results discussed above, we are therefore formed the view that, the N_{TB} phase behaviour difference between symmetric and asymmetric dimers could be accounted for by the distinct hybridization of sulfur/oxygen and subsequent influences on molecular shape, *i.e.* the opening angle and rotational angle of the dimers.

Conclusions

In summary, we have shown that resonant scattering, TReXS in particular, can be a unique tool to decipher the molecular orientation arrangement in helical liquid crystals. Using this methodology we arrived at an explanation of the N_{TB} phase behaviour difference between symmetric and asymmetric dimers in the perspective of hybridization, which should be universal for other dimer systems and inspiring for molecular design as well as chirality generation. Furthermore, we demonstrated that the dramatic enhancement of the resonant peak in the N_{TB}, when approaching the sulfur K-edge, can be well accounted for using the energy-dependence of complex form factors, which can be extracted from X-ray absorption spectroscopy measurements. This opens a way to predict resonant scattering patterns of newly proposed structural models, where molecular orientation varies periodically in space. We anticipate that this methodology can be readily applied to obtain new insights of the self-assembly of the mysterious polarization modulated $SmAPF_{mod}$ phase in bent-core liquid crystals[70], the twist grain boundary smectics[71] and other emerging complex hierarchical structures. Moreover, this methodology can potentially be used in characterization of nano-electro-mechanical systems[72] and other soft robotics. With quick experimental absorption spectroscopy measurement, model-dependent resonant X-ray scattering patterns can be computed in advance, which will greatly speed up the process of materials discovery.

Author contributions

F.L. and C.Z. initialized the project. Y.C. carried out the TReXS measurement under the guidance of F.L. and C.Z. and with help of J.F. . Y.C. carried out DFT calculation under guidance of H.Z.. Y.A. and K.Z. offer the materials. Y.C. analysed the experimental data. A.N. helped in analysing and discussing the results. Y.C., G.H.M., F.L. and C.Z. wrote the paper with inputs from all authors.

Conflicts of interest

There are no conflicts to declare.

Acknowledgements

The work is supported by National Natural Science Foundation of China (No. 21774099, 21761132033 and 51603166), Science and Technology Agency of Shaanxi Province (2016KW-050 and 2018KWZ-03) and the 111 Project 2.0 (BP2018008). Y.C. thanks China Scholarship Council (CSC) for providing financial support (201706280170). We also thank Dr. Eric Gullikson at CXRO, LBNL and Dr. Howard Padmore at ALS, LBNL, for helpful discussions. We acknowledge use of Beamlines 5.3.1 of the Advanced Light Source supported by the Director of the Office of Science, Office of Basic Energy Sciences, of the U.S. Department of Energy under contract no. DE-AC02-05CH11231.

Notes and references

1. J. C. Marini, S. D. Levene, D. M. Crothers and P. T. Englund, *Proc. Natl Acad. Sci. USA*, 1982, **79**, 7664-7668.
2. N. Tamaoki, *Adv. Mater.*, 2001, **13**, 1135-1147.
3. J. R. Barnett and V. A. Bonham, *Biol. Rev.*, 2004, **79**, 461-472.
4. D.-K. Yang, *Fundamentals of liquid crystal devices*, John Wiley & Sons, 2014.
5. R. Balian, *Houches Lectures, 1973: Molecular Fluids*, Routledge, 1976.

6. P. Barnes, A. Douglass, S. Heeks and G. Luckhurst, *Liq. Cryst.*, 1993, **13**, 603-613.
7. I. Dozov, *Europhys. Lett.*, 2001, **56**, 247-253.
8. R. Memmer, *Liq. Cryst.*, 2002, **29**, 483-496.
9. V. Panov, M. Nagaraj, J. Vij, Y. P. Panarin, A. Kohlmeier, M. Tamba, R. Lewis and G. Mehl, *Phys. Rev. Lett.*, 2010, **105**, 167801.
10. M. Cestari, S. Diez-Berart, D. A. Dunmur, A. Ferrarini, M. R. de la Fuente, D. J. B. Jackson, D. O. Lopez, G. R. Luckhurst, M. A. Perez-Jubindo, R. M. Richardson, J. Salud, B. A. Timimi and H. Zimmermann, *Phys. Rev. E: Stat. Nonlinear, Soft Matter Phys.*, 2011, **84**, 031704.
11. M. Cestari, E. Frezza, A. Ferrarini and G. R. Luckhurst, *J. Mater. Chem.*, 2011, **21**, 12303-12308.
12. P. A. Henderson and C. T. Imrie, *Liq. Cryst.*, 2011, **38**, 1407-1414.
13. L. Beguin, J. W. Emsley, M. Lelli, A. Lesage, G. R. Luckhurst, B. A. Timimi and H. Zimmermann, *J. Phys. Chem. B*, 2012, **116**, 7940-7951.
14. V. Borshch, Y.-K. Kim, J. Xiang, M. Gao, A. Jákli, V. P. Panov, J. K. Vij, C. T. Imrie, M.-G. Tamba and G. H. Mehl, *Nat. Commun.*, 2013, **4**, 2635.
15. D. Chen, J. H. Porada, J. B. Hooper, A. Klittnick, Y. Shen, M. R. Tuchband, E. Korblova, D. Bedrov, D. M. Walba, M. A. Glaser, J. E. Maclennan and N. A. Clark, *Proc. Natl Acad. Sci. USA*, 2013, **110**, 15931-15936.
16. C. Greco, G. R. Luckhurst and A. Ferrarini, *Soft Matter*, 2014, **10**, 9318-9323.
17. E. G. Virga, *Phys. Rev. E: Stat. Nonlinear, Soft Matter Phys.*, 2014, **89**, 052502.
18. V. Panov, R. Balachandran, M. Nagaraj, J. Vij, M. Tamba, A. Kohlmeier and G. Mehl, *Appl. Phys. Lett.*, 2011, **99**, 261903.
19. V. Panov, R. Balachandran, J. Vij, M. Tamba, A. Kohlmeier and G. Mehl, *Appl. Phys. Lett.*, 2012, **101**, 234106.
20. C. Meyer, G. Luckhurst and I. Dozov, *Phys. Rev. Lett.*, 2013, **111**, 067801.
21. J. Xiang, S. V. Shiyanovskii, C. Imrie and O. D. Lavrentovich, *Phys. Rev. Lett.*, 2014, **112**, 217801.
22. E. Gorecka, M. Salamonczyk, A. Zep, D. Pociecha, C. Welch, Z. Ahmed and G. H. Mehl, *Liq. Cryst.*, 2015, **42**, 1-7.
23. Z. Zhang, V. P. Panov, M. Nagaraj, R. J. Mandle, J. W. Goodby, G. R. Luckhurst, J. C. Jones and H. F. Gleeson, *J. Mater. Chem. C*, 2015, **3**, 10007-10016.
24. K. Adlem, M. Čopič, G. Luckhurst, A. Mertelj, O. Parri, R. Richardson, B. Snow, B. Timimi, R. Tuffin and D. Wilkes, *Phys. Rev. E: Stat. Nonlinear, Soft Matter Phys.*, 2013, **88**, 022503.
25. C. Zhu, M. R. Tuchband, A. Young, M. Shuai, A. Scarbrough, D. M. Walba, J. E. Maclennan, C. Wang, A. Hexemer and N. A. Clark, *Phys. Rev. Lett.*, 2016, **116**, 147803.
26. W. Stevenson, Z. Ahmed, X. Zeng, C. Welch, G. Ungar and G. Mehl, *Phys. Chem. Chem. Phys.*, 2017, **19**, 13449-13454.
27. M. R. Tuchband, D. A. Paterson, M. Salamończyk, V. A. Norman, A. N. Scarbrough, E. Forsyth, E. Garcia, C. Wang, J. M. Storey, D. M. Walba, S. Sprunt, A. Jakli, C. Zhu, C. T. Imrie and N. A. Clark, *Proc. Natl Acad. Sci. USA*, 2019, **116**, 10698-10704.
28. W. D. Stevenson, X. Zeng, C. Welch, A. K. Thakur, G. Ungar and G. H. Mehl, *J. Mater. Chem. C*, 2020, **8**, 1041-1047.
29. A. G. Vanakaras and D. J. Photinos, *Soft Matter*, 2016, **12**, 2208-2220.
30. A. G. Vanakaras and D. J. Photinos, *Liq. Cryst.*, 2018, **45**, 2184-2196.
31. J. Shi, H. Sidky and J. K. Whitmer, *Soft Matter*, 2019, **15**, 8219-8226.
32. L. M. Heist, E. T. Samulski, C. Welch, Z. Ahmed, G. H. Mehl, A. G. Vanakaras and D. J. Photinos, *Liq. Cryst.*, 2020, **47**, 2058-2073.
33. M. Salamończyk, N. Vaupotič, D. Pociecha, C. Wang, C. Zhu and E. Gorecka, *Soft Matter*, 2017, **13**, 6694-6699.
34. M. R. Tuchband, M. Shuai, K. A. Graber, D. Chen, C. Zhu, L. Radzihovsky, A. Klittnick, L. M. Foley, A. Scarbrough, J. H. Porada, M. Moran, J. Yelk, D. Bedrov, E. Korblova, D. M. Walba, A. Hexemer, J. E. Maclennan, M. A. Glaser and N. A. Clark, *arXiv preprint arXiv:1703.10787*, 2017.
35. A. Aluculesei, H. Cachitas, J. Carvalho, F. V. Chavez, J. L. Figueirinhas, P. J. Sebastião, C. Cruz, M. G. Tamba, A. Kohlmeier and G. H. Mehl, *Phys. Chem. Chem. Phys.*, 2019, **21**, 4523-4537.
36. N. Dingenouts, R. Merkle, X. Guo, T. Narayanan, G. Goerigk and M. Ballauff, *J. Appl. Crystallogr.*, 2003, **36**, 578-582.
37. K. Krishnamoorthy, K. Hoffmann, S. Kewalramani, J. D. Brodin, L. M. Moreau, C. A. Mirkin, M. Olvera de la Cruz and M. J. Bedzyk, *ACS Cent. Sci.*, 2018, **4**, 378-386.
38. C. Wang, D. H. Lee, A. Hexemer, M. I. Kim, W. Zhao, H. Hasegawa, H. Ade and T. P. Russell, *Nano Lett.*, 2011, **11**, 3906-3911.
39. B. A. Collins, J. E. Cochran, H. Yan, E. Gann, C. Hub, R. Fink, C. Wang, T. Schuettfort, C. R. McNeill, M. L. Chabinyc and H. Ade, *Nat. Mater.*, 2012, **11**, 536-543.
40. J. R. Tumbleston, B. A. Collins, L. Yang, A. C. Stuart, E. Gann, W. Ma, W. You and H. Ade, *Nat. Photonics*, 2014, **8**, 385-391.
41. Y. Cao, C. Feng, A. Jakli, C. Zhu and F. Liu, *Giant*, 2020, **2**, 100018.
42. C. Zhu, C. Wang, A. Young, F. Liu, I. Gunkel, D. Chen, D. Walba, J. Maclennan, N. Clark and A. Hexemer, *Nano Lett.*, 2015, **15**, 3420-3424.
43. Y. Cao, M. Alaasar, A. Nallapaneni, M. Salamończyk, P. Marinko, E. Gorecka, C. Tschierske, F. Liu, N. Vaupotič and C. Zhu, *Phys. Rev. Lett.*, 2020, **125**, 027801.
44. J. P. Abberley, R. Killah, R. Walker, J. M. Storey, C. T. Imrie, M. Salamończyk, C. Zhu, E. Gorecka and D. Pociecha, *Nat. Commun.*, 2018, **9**, 1-7.
45. M. T. Murachver, A. Nemati, M. Salamonczyk, C. Bullock, Z. Sabata, H. Rahmani, T. Vorobiova, A. Izadnegandar, S. M. Salili, V. Norman, C. Zhu, T. Hegmann, S. N. Sprunt, J. T. Gleeson and A. I. Jakli, *Soft Matter*, 2019, **15**, 3283-3290.
46. M. Salamończyk, N. Vaupotič, D. Pociecha, R. Walker, J. M. Storey, C. T. Imrie, C. Wang, C. Zhu and E. Gorecka, *Nat. Commun.*, 2019, **10**, 1922.
47. B. L. Henke, E. M. Gullikson and J. C. Davis, *At. Data Nucl. Data Tables*, 1993, **54**, 181-342.
48. P. Mach, R. Pindak, A.-M. Levelut, P. Barois, H. Nguyen, C. Huang and L. Furenlid, *Phys. Rev. Lett.*, 1998, **81**, 1015-1018.
49. S. Wang, L. Pan, R. Pindak, Z. Liu, H. Nguyen and C.-C. Huang, *Phys. Rev. Lett.*, 2010, **104**, 027801.
50. M. Salamończyk, R. J. Mandle, A. Makal, A. Liebman-Peláez, J. Feng, J. W. Goodby and C. Zhu, *Soft Matter*, 2018, **14**, 9760-9763.

51. C. Feng, J. Feng, R. Saha, Y. Arakawa, J. Gleeson, S. Sprunt, C. Zhu and A. Jákli, *Physical Review Research*, 2020, **2**, 032004.
52. J. Ilavsky, *J. Appl. Crystallogr.*, 2012, **45**, 324-328.
53. R. J. Pandolfi, D. B. Allan, E. Arenholz, L. Barroso-Luque, S. I. Campbell, T. A. Caswell, A. Blair, F. De Carlo, S. Fackler and A. P. Fournier, *J. Synchrotron. Radiat*, 2018, **25**, 1261-1270.
54. Y. Arakawa, K. Komatsu and H. Tsuji, *New J. Chem.*, 2019, **43**, 6786-6793.
55. E. Cruickshank, M. Salamończyk, D. Pociecha, G. J. Strachan, J. M. Storey, C. Wang, J. Feng, C. Zhu, E. Gorecka and C. T. Imrie, *Liq. Cryst.*, 2019, **46**, 1595-1609.
56. H. Monobe, L. An, P. Hu, B.-Q. Wang, K.-Q. Zhao and Y. Shimizu, *Mol. Cryst. Liq. Cryst*, 2017, **647**, 119-126.
57. K. R. de L, *J. Opt. Soc. Am*, 1926, **12**, 547-557.
58. V. Belyakov and V. E. Dmitrienko, *Sov. Phys. Usp.*, 1985, **28**, 535-562.
59. D. Templeton and L. Templeton, *"Acta Crystallogr., Sect. A: Found. Crystallogr."*, 1985, **41**, 133-142.
60. A.-M. Levelut and B. Pansu, *Phys. Rev. E: Stat. Nonlinear, Soft Matter Phys.*, 1999, **60**, 6803-6815.
61. T. Araki, H. Ade, J. M. Stubbs, D. C. Sundberg, G. E. Mitchell, J. B. Kortright and A. Kilcoyne, *Appl. Phys. Lett.*, 2006, **89**, 124106.
62. A. Cady, R. Pindak, W. Caliebe, P. Barois, W. Weissflog, H. Nguyen and C. Huang, *Liq. Cryst.*, 2002, **29**, 1101-1104.
63. H. F. Gleeson and L. S. Hirst, *ChemPhysChem*, 2006, **7**, 321-328.
64. Y. Takanishi, Y. Ohtsuka, Y. Takahashi and A. Iida, *Phys. Rev. E: Stat. Nonlinear, Soft Matter Phys.*, 2010, **81**, 011701.
65. R. Saha, C. Feng, C. Welch, G. H. Mehl, J. Feng, C. Zhu, J. Gleeson, S. Sprunt and A. Jákli, *Phys. Chem. Chem. Phys.*, 2021, **23**, 4055-4063.
66. R. J. Mandle, C. T. Archbold, J. P. Sarju, J. L. Andrews and J. W. Goodby, *Sci. Rep.*, 2016, **6**.
67. D. A. Paterson, M. Gao, Y.-K. Kim, A. Jamali, K. L. Finley, B. Robles-Hernandez, S. Diez-Berart, J. Salud, M. Rosario de la Fuente, B. A. Timimi, H. Zimmermann, C. Greco, A. Ferrarini, J. M. D. Storey, D. O. Lopez, O. D. Lavrentovich, G. R. Luckhurst and C. T. Imrie, *Soft Matter*, 2016, **12**, 6827-6840.
68. J. W. Emsley, G. De Luca, A. Lesage, D. Merlet and G. Pileio, *Liq. Cryst.*, 2007, **34**, 1071-1093.
69. R. J. Mandle and J. W. Goodby, *Soft Matter*, 2016, **12**, 1436-1443.
70. C. Zhu, R. Shao, R. A. Reddy, D. Chen, Y. Shen, T. Gong, M. A. Glaser, E. Korblova, P. Rudquist, J. E. Maclennan, D. M. Walba and N. A. Clark, *J. Am. Chem. Soc.*, 2012, **134**, 9681-9687.
71. J. Fernsler, L. Hough, R. F. Shao, J. E. Maclennan, L. Navailles, M. Brunet, N. V. Madhusudana, O. Mondain-Monval, C. Boyer, J. Zasadzinski, J. A. Rego, D. M. Walba and N. A. Clark, *Proc. Natl Acad. Sci. USA*, 2005, **102**, 14191-14196.
72. G. Huang and Y. Mei, *J. Materiomics*, 2015, **1**, 296-306.